





Continuous Fast Terminal Sliding Surface-Based Sensorless Speed Control of PMBLDCM Drive

Prashant Kumar , Member, IEEE, Devara Vijaya Bhaskar , Senior Member, IEEE, Ranjan Kumar Behera , Senior Member, IEEE, and Utkal Ranjan Muduli , Senior Member, IEEE

Abstract—Variable frequency drives (VFDs) have been used for position sensors for many years. Alternatively, reliable VFDs for smart autonomous systems require the simultaneous configuration of sensors and sensorless operation. This article details the design and implementation of a continuous fast terminal (CFT) sliding mode controller (SMC)-based speed controller and speed estimation through the CFT sliding mode observer that accounts for iron loss while calculating total disturbances. The rotor speed dynamics of the permanent magnet brushless dc motor drive system is first investigated considering lumped disruption (interference, parametric complexity, and non-linear dynamics). The built-in SMC can control the rotor speed in real time, as well as analyze and compensate for aggregated interruptions in rotor speed dynamics. In addition, the field-oriented control (FOC) method is developed to maximize torque production while drastically minimizing torque ripples. With this approach, the zero-torque pulsation constraint is gradually achieved at a wide speed range. The validation of the proposed CFT-SMC with FOC is carried out using simulation and experiments. According to the comparative study, the proposed sensorless control outperforms conventional methods due to the inclusion of iron loss.

Index Terms—Continuous fast terminal (CFT), permanent magnet brushless dc motor (PMBLDCM), sensorless field-oriented control, sliding mode controller (SMC), torque ripple, voltage source inverter (VSI).

I. INTRODUCTION

LOW-POWERED electric vehicles and high-precision industrial applications benefit from permanent magnet brushless dc motors (PMBLDCM) [1]. In addition to improving the torque-speed characteristics, the application would also

increase the torque–weight ratio, improve control sensitivity, and reduce vibration. As a result of magnetic alignment and winding configuration, PMBLDCM is characterized by a trapezoidal back electromagnetic force (EMF), which demands a specific control strategy to maintain the electromagnetic torque. Normally, PMBLDCM works in a six-step conduction mode, commuting the voltage source inverter (VSI) every 60 electrical degrees. Meanwhile, PMBLDCM exhibits a torque ripple during operation, specifically a periodic commutation torque ripple, which is crucial to ensure smooth operation [2]. In high-precision applications, torque ripple causes vibrations and acoustic noise. In addition, the torque ripple causes more current ripples and higher copper losses in the PMBLDCM drive, resulting in a reduction in the overall drive efficiency. Consequently, reducing copper loss is a significant focus of current research to improve motor torque performance with reduced torque ripple [3].

An accurate PMBLDCM modeling, in which material and design parameters are taken into account, is essential to reduce torque ripple [4]. Permanent magnets are particularly susceptible to performance degradation due to temperature and magnetic saturation [5]. A decrease in PMBLDCM performance is attributed to iron loss when hysteresis and eddy current losses are considered [6]. In the literature, a variety of PMBLDCM models based on iron loss are examined to predict and assess the effects of iron loss [3]. Iron loss directly or indirectly affects the electromagnetic torque performance of the PMBLDCM drive [7]. Therefore, a desirable electromagnetic torque reference must be evaluated to compensate for the effect of iron loss. Electromagnetic torque reference is traditionally generated from a proportional–integral (PI)-based speed regulator with a motor-dependent gain factor [8]. This stage of outer loop control does not include any iron loss compensation. It is only possible that the speed feedback should be included with the disturbance corresponding to iron loss. This type of disturbance inclusion may not be possible with traditional rotor position sensor implementation. Again, the reliability and sensitivity of the rotor position sensor have a significant impact on the performance of PMBLDCM [2], [9]. This challenge of sensitivity can be overcome by high-quality encoders and resolvers in electrical drives for the electric vehicle propulsion system. However, sensor devices are sensitive to mechanical and electrical malfunctions, susceptible to electromagnetic interference [6], which could also cause the vehicle to go out of operation or sometimes lead to severe situations. Therefore, this motivates the research

Manuscript received 21 April 2022; revised 6 August 2022 and 28 October 2022; accepted 23 November 2022. Date of publication 6 December 2022; date of current version 17 April 2023. This work was supported by the Science and Engineering Research Board (SERB), Government of India, under Grant EEQ/2021/000119. (Corresponding authors: Devara Vijaya Bhaskar; Utkal Ranjan Muduli.)

Prashant Kumar and Devara Vijaya Bhaskar are with the Department of Electrical Engineering, IIT (ISM) Dhanbad, Dhanbad 826004, India (e-mail: prashant.18dr0100@ee.iitism.ac.in; devara@iitism.ac.in).

Ranjan Kumar Behera is with the Department of Electrical Engineering, Indian Institute of Technology, Patna, 801103, India (e-mail: rkb@iitp.ac.in).

Utkal Ranjan Muduli is with the Advanced Power and Energy Center, Department of Electrical Engineering and Computer Science, Khalifa University, Abu Dhabi 127788, UAE (e-mail: utkal.muduli@ku.ac.ae).

Color versions of one or more figures in this article are available at <https://doi.org/10.1109/TIE.2022.3225850>.

Digital Object Identifier 10.1109/TIE.2022.3225850

demand for sensorless motor drive operation that includes iron loss compensation [10].

Rotor speed dynamics is a time-varying nonlinear mechanism that is attributed to lumped disturbances [11]. These external disturbances constitute the load torque, the friction torque, and the uncertainties of the parameters. Adopting a traditional controller to address the problem of rotor speed tracking in the PMBLDCM drive system results in poor dynamic response [12]. Therefore, it is effective to utilize the nonlinear control technique that incorporates external disturbances and large nonlinear effects to achieve robust rotor speed control [13]. Sliding mode observer (SMO)-based rotor position estimation to achieve sensorless operation can positively contribute to enhance the reliability and drives performance. Due to the superior ability to maintain good dynamic performance and improve the ability to reject disturbances, the SMO is deployed in [14]. In the conventional SMO method, a higher switching gain is required to approach the maximum limit of total disturbance, causing steady error and chattering. After analyzing the state-of-the-art SMO for PMBLDCM speed estimation, it can be concluded that the PMBLDCM control problem remains a relatively open topic and requires further research. Hence, the objectives of this article are as follows.

- 1) To develop an SMO for PMBLDCM speed estimation with improved disturbance rejection capability for better stability. For this, precise dynamic modeling of the PMBLDCM containing parameters and load torque is required for accurate performance.
- 2) To generate continuous control signals and eliminate the chattering phenomenon of the SMO.
- 3) To achieve fast time convergence of the sliding surface to the equilibrium state in a specific time limit.

SMO is often used as a nonlinear control theory as a result of its desirable advantages, such as stability toward mismatched perturbations and reduced-order compensated dynamics [15]. As a result, the SMO-based speed controller [i.e., sliding mode controller (SMC)] has gained considerable interest [16]. SMC takes the change in load torque as a disturbance for PMBLDCM [17]. However, this article used hall sensors where the use of sensors has several limitations. Fuzzy SMC for PMBLDCM with linear sliding surface and switching gain function is proposed in [18]. Due to the linear surface of traditional SMC and asymptotic stability problems with higher switching gain, it cannot be considered a robust feature for PMBLDCM applications [15]. Furthermore, fuzzy SMC is reported using an integral sliding surface for electric vehicle application [11], for water pump application [19] using PMBLDCM. Conventional SMCs demand a level of control gain to improve effective accuracy and stability, even though they have considerable chattering issues [12]. To overcome the stability problem, the controller is built by reconfiguring the sliding surface of the traditional SMC approach. Terminal SMC (TSMC) and nonsingular fast TSMC (FTSMC) for permanent magnet synchronous motor (PMSM) are explored in [20] and [21], respectively. The TSMC approach, among all other sliding procedures devised to deal with this problem, ensures limited time convergence while monitoring errors to the origin [22]. However, TSMC has the limitation

of discontinuous control action, leading to the chattering phenomenon. To reduce such issues, a nonsingular FTSMC for the automotive throttle system is reported in [21], [23], and [24]. Therefore, the objectives of this article are extended further to the following:

- 1) design high-precision speed tracking through SMC, considering the effect of iron loss and unknown external disturbance and
- 2) improve the torque ripple content during steady-state dynamics and transient conditions, considering a better speed profile at low stator phase currents total harmonic distortion (THD).

Without a suitable control action, PMBLDCM with iron loss consideration prevails in instability and disruption [7]. This often results in ineffective closed-loop control performance, such as increased torque ripple and reduced speed. Several sensorless high-performance control strategies, such as field-oriented control (FOC) [25], direct torque control (DTC) [26], and SMC [11], are proposed to control the PMBLDCM speed. A three-level neutral point clamped (NPC) VSI-based torque ripple suppression circuit is proposed in [27]. This approach reduces the commutation torque ripple at both low and high speeds, but requires a high switching frequency. In [28], a finite control set model predictive control approach was presented, which provides a fast torque response and good steady-state performance; however, it is completely dependent on motor parameters. FOC method presented in [25] provides satisfactory performance with a reduced torque ripple. This method is completely derived as a parameter-dependent strategy that can degrade the performance of the drive with variation in the operating motor parameters. Therefore, a sensorless FOC scheme is proposed to address the issues resulting from variations in internal parameters and unknown external disturbances. Sensorless FOC offers significant benefits in terms of efficiency and torque quality if the precise angular rotor orientation signal of PMBLDCM is available. To make the technique acceptable for implementation to achieve the exact rotor position, the SMO is integrated into an FOC architecture that guarantees a stable system with reduced computational burden. During PMBLDCM drive control, the objective is to achieve maximum torque per ampere (MTPA) while regulating the currents in the synchronously rotating dq -frame. The complete cycles of the electrical rotor angle are divided into six sectors to execute this procedure. In each sector, pulsewidth modulated (PWM) signals are used to regulate one leg of the VSI at a specified duty cycle, whereas a fixed voltage (usually low) is used for the other. In the proposed sensorless FOC, a prerequisite parameter information or monitoring system is required specifically for SMO, which is again considered as a disturbance if any parameter variation occurs during motor operation. The significant contributions of this article can be summarized as follows.

- 1) Dynamic modeling with the FOC controller is suggested for the speed control of the PMBLDCM drives, which yields better system stability considering the effect of iron loss. The MTPA control is achieved with the suggested FOC controller that is independent of parameter variation.

Step 1: Initially, the dc-Link voltage v_{dc} and a-phase and b-phase stator currents i_s^{ab} are measured using one voltage sensor and two current sensors.

Step 2: The voltages (v_s^{abc}) in the stator phases are formulated using the VSI model, that is, $v_s^{abc} = \pm 0.5 S^{abc} v_{dc}$. Here, S^{abc} and $S^{a'b'c'}$ are the switching pulses and their complements to control the IGBT switches, as shown in Fig. 1. Internally, S^{abc} is used as feedback through a unit delay. The c-phase current can be generated by the relation $i_s^c = -(i_s^a + i_s^b)$. After generating phase voltages and phase currents, v_s^{dq} and i_s^{dq} can be generated using the following equation, considering the generic variable $X \in \{v_s, i_s\}$:

$$X^{dq} = X^d + jX^q = e^{-j\hat{\theta}_r} \sqrt{\frac{2}{3}} \sum_{\substack{k=1 \\ l \in \{a,b,c\}}}^3 X^l e^{j\frac{2\pi}{3}(k-1)}. \quad (4)$$

Step 3: Here, $\hat{\theta}_r$ is the estimated value of the position of the PMBLDCM rotor, which is generated from the CFT-SMO described in Section III-C. CFT-SMO also evaluates the estimated value of the rotor angular speed ($\hat{\omega}_m$). The inputs to the CFT-SMO are v_s^{dq} , i_s^{dq} , and the known disturbance, as shown in Fig. 1.

Step 4: The estimated value of $\hat{\omega}_m$ is compared with the reference value of the angular speed of the rotor (ω_m^*), and the corresponding speed tracking error ($\varepsilon_\omega = \omega_m^* - \hat{\omega}_m$) is controlled by a CFT-SMC as designed in Section III-B. CFT-SMC also generates the q -axis reference current i_s^{q*} . The electromagnetic torque (T_{em}) vary linearly with i_s^{q*} , the desired torque for PMBLDCM can be generated through i_s^{q*} control by maintaining d -axis reference current (i_s^{d*}) to zero, i.e., $i_s^{d*} = 0$.

Step 5: Utilize two separate PI regulators to track current error ε_i^{dq} (i.e., $[\varepsilon_i^q, \varepsilon_i^d]$), which further produces v_s^{q*} and v_s^{d*} , respectively. k_p^d and k_i^d (k_p^q and k_i^q) are the proportional and integral constants of the d -axis (q -axis) current controller, respectively.

Step 6: Convert the reference voltage space vector ($\vec{v}_s^{dq*} = v_s^{d*} + jv_s^{q*}$) to $\vec{v}_s^{\alpha\beta*}$ as the following using the estimated rotor angle $\hat{\theta}_r$:

$$\vec{v}_s^{\alpha\beta*} = |\vec{v}_s^{\alpha\beta*}| e^{j\delta_v} = \vec{v}_s^{dq*} e^{j\hat{\theta}_r} \quad (5)$$

where $\vec{v}_s^{\alpha\beta*}$ is utilized further to calculate the sector (k_v) and the dwell angle (δ_v).

Step 7: k_v and δ_v are used to select the appropriate voltage vectors as in the SVPWM scheme [30] and the switching pulses $\{S^{abc}, S^{a'b'c'}\}$ are generated accordingly to ensure the operation of the constant switching frequency.

III. PMBLDCM SPEED ESTIMATION AND CONTROL WITH IRON LOSS CONSIDERATION

To achieve higher steady-state tracking accuracy with a faster response, a CFT SMC is presented in this section. Initially, the robustness of CFT-SMC is analyzed to estimate external disturbances through dynamic modeling of PMBLDCM. In addition, a simplified implementation methodology is incorporated to understand the design flow of the proposed CFT-SMC. In this section, a stability analysis is provided to see the feasibility of the proposed method.

A. PMBLDCM Torque and Speed Dynamics

The effective electromagnetic torque (T_{em}) developed can be represented as (6). It can be seen that T_{em} is completely determined by the flux linkage and the magnetizing component of the current

$$T_{em} = \Re(\bar{\lambda}_s^{dq} i_m^{dq}) = \Re(C \bar{\lambda}_s^{dq} i_s^{dq}) - T_i \quad (6)$$

where $\bar{\{\}}\}$ and $\Re\{\}$ represent the complex conjugate and the real part of a complex variable, respectively. Without considering the effect of iron loss, the abovementioned electromagnetic torque can be modeled as follows:

$$T_{em} = T_{eS} = \Re(\bar{\lambda}_s^{dq} i_s^{dq}) = \lambda_s^{d;d} + \lambda_s^{q;q}. \quad (7)$$

It means that the term T_i in (6) represents an additional torque component, which is introduced by considering the effect of iron loss. Now, the iron loss torque component T_i can be formulated as follows:

$$T_i|_{S_1, \dots, S_6} = \frac{\omega_m}{R_i} |\lambda_s^{dq}|_{S_1, \dots, S_6}^2 \quad (8)$$

where $k_v \in \{S_1 \dots S_6\}$ represents the sectors of the PMBLDCM back-EMF space vector. Taking into account the characteristics of the system and the load torque, the design of a high-precision speed tracking controller will be a challenging task. FOC essentially involves the regulation of rotational variation between the stator and rotor flux vectors to maximize torque. The FOC technique described in Section II-B has two inner current control loops and one outer speed control loop. By generating a reference current from the outer loop, the inner loop can be controlled. Considering that T_{em} is a linear function of the q -axis current (i_s^q), it is possible to generate a constant torque by regulating the current on the q -axis while maintaining the zero value of d -axis current (i_s^d), i.e., $i_s^d = 0$. Now, the electromagnetic torque T_{em} can be expressed in terms of the current (i_s^q) on the q -axis as follows:

$$T_{em} = k_t i_s^q - T_i \quad (9)$$

where k_t is denoted as the torque constant considering the iron loss effect, and its value can be represented as follows:

$$k_t = k_c |\lambda_s^{dq}| \sin(\theta_r + \theta_c). \quad (10)$$

Ignoring mechanical losses, the mechanical dynamic of PMBLDCM in terms of T_{em} can be described as follows:

$$T_{em} = J \dot{\omega}_m + B \omega_m + T_L \quad (11)$$

where J , B , and T_L represent the moment of inertia, the damping coefficient, and the applied load torque, respectively. Let $\hat{\omega}_m$ be the estimated angular speed of PMBLDCM. Finally, by solving (9) and (11), the rate of change in angular speed can be interpreted as follows:

$$\dot{\omega}_m = \frac{1}{J} T_{em} - \frac{1}{J} T_L - \frac{B}{J} \omega_m = b_i i_s^{q*} - f_\omega^m \quad (12)$$

where $b_i (=k_t/J)$ is considered as control gain and $f_\omega^m (= (k_t(i_s^{q*} - i_s^q) + T_i + T_L + B\omega_m)/J)$ is the total disturbance due to unknown disturbances and unmodeled dynamics.

B. CFT-SMC Proposed Design

Consider that the speed tracking error (ε_ω) as the difference between the reference speed ω_m^* and the estimated speed $\hat{\omega}_m$ of PMBLDCM, i.e., $\varepsilon_\omega = \omega_m^* - \hat{\omega}_m$. Now, the dynamics of the speed tracking error can be expressed as (13). The objective of calculating (13) is to minimize the speed error close to zero.

$$\dot{\varepsilon}_\omega = \dot{\omega}_m^* - \dot{\hat{\omega}}_m. \quad (13)$$

Solving (12) and (13), $\dot{\varepsilon}_\omega$ can be further simplified as follows:

$$\dot{\varepsilon}_\omega = \dot{\omega}_m^* - b_i i_s^{q*} + f_\omega^m. \quad (14)$$

The sliding surface (s) of conventional SMC, TSMC, and NTSMC can be mentioned as follows:

$$s = \dot{\varepsilon}_\omega + \mu \varepsilon_\omega, \quad \mu > 0 \quad (\text{SMC}) \quad (15)$$

$$s = \dot{\varepsilon}_\omega + \mu \varepsilon_\omega^\delta, \quad \mu > 0, 0 < \delta < 1 \quad (\text{TSMC}) \quad (16)$$

$$s = \varepsilon_\omega + \mu \dot{\varepsilon}_\omega^\delta, \quad \mu > 0, 0 < \delta < 1 \quad (\text{NTSMC}). \quad (17)$$

The TSMC has a slower convergence rate than the SMC when the value of δ is taken into account. The NTSMC has a slower convergence rate but can help to avoid singularity issues when the states are distant from the equilibrium point. To improve the convergence rate against disturbances, the CFT-SMC is developed as indicated by

$$s = \dot{\varepsilon}_\omega + \mu_1 |\dot{\varepsilon}_\omega|^{\delta_1} \text{sgn}(\dot{\varepsilon}_\omega) + \mu_2 |\varepsilon_\omega|^{\delta_2} \text{sgn}(\varepsilon_\omega) \quad (18)$$

where conditions $\mu_1, \mu_2 > 0$, $0 < \delta_1, \delta_2 < 2$, $\delta_2 > \delta_1$ are satisfied. The operator $\text{sgn}(\ast)$ represents the signum function and can be defined as follows:

$$\text{sgn}(\ast) = \begin{cases} +1, & \ast > 0 \\ \in [-1, +1], & \ast = 0 \\ -1, & \ast < 0. \end{cases} \quad (19)$$

Let the dynamics of the sliding surface of the CFT be defined as follows:

$$\dot{s} = -k_1 s - k_2 |s|^{\delta_3} \text{sgn}(s) \quad (20)$$

where conditions $k_1, k_2 > 0$ and $0 < \delta_3 < 1$ are satisfied. Now, the integral form of (20) can be obtained as follows:

$$s = \int_0^t \left[-k_1 s - k_2 |s|^{\delta_3} \text{sgn}(s) \right] dt. \quad (21)$$

By solving (14), (18), and (21), the control input (i_s^{q*}) can be obtained as follows:

$$i_s^{q*} = b_i^{-1} (\dot{\omega}_m^* + \chi_1 + \chi_2 + f_\omega^m) \quad (22)$$

$$\chi_1 = \mu_1 |\dot{\varepsilon}_\omega|^{\delta_1} \text{sgn}(\dot{\varepsilon}_\omega) + \mu_2 |\varepsilon_\omega|^{\delta_2} \text{sgn}(\varepsilon_\omega) \quad (23)$$

$$\chi_2 = \int_0^t \left[k_1 s + k_2 |s|^{\delta_3} \text{sgn}(s) \right] dt. \quad (24)$$

Furthermore, i_s^{q*} can be used for the FOC scheme, as mentioned in Section II-B. The detailed block diagram approach to develop i_s^{q*} is shown in Fig. 3. Here, tracking differentiator (TD) is represented as the tracking differentiator, which utilizes the Euler forward approximation.

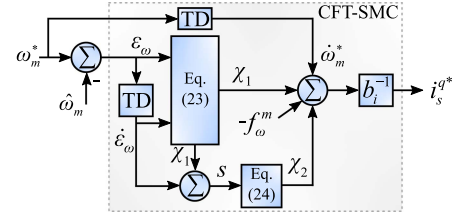


Fig. 3. CFT-SMC structure for PMBLDCM speed regulation system.

B. Stability Analysis:

The sliding surface and the control law are two distinct phases in the construction of an SMC controller. On the other hand, the control law can cause chattering in the system, which is crucial in the design of SMCs. The SMC demands a low control gain to reduce the chattering phenomenon. In contrast, a large control gain is necessary to ensure that the SMC is adaptable to massive disturbances with minimal undesirable chattering issue. An attractive solution to this challenge is to make the SMC control law adaptable to measured disturbances. To converge the speed tracking error in (13) to zero, it is necessary to satisfy the SMC reachability criteria in the following:

$$s\dot{s} < 0 \quad \text{and} \quad s \rightarrow 0. \quad (25)$$

To determine the range of coefficients in the SMC, the stability of the designed SMC should be analyzed. Thus, the Lyapunov stability function is described in the following to prove the stability of the improved CFT-SMC:

$$V = \frac{1}{2} s^2. \quad (26)$$

Now, the dynamics of the Lyapunov stability function can be derived in the following using (20):

$$\dot{V} = s\dot{s} = -k_1 s^2 - k_2 |s|^{\delta_3+1} \text{sgn}(s). \quad (27)$$

The dynamics of the PMBLDCM speed error converges to zero in finite time if (25) satisfies, i.e., $\dot{V} < 0$. Now, (27) can be rewritten as follows:

$$\begin{aligned} \dot{V} &\leq -k_1 s^2 - k_2 |s|^{\delta_3+1} \\ &\leq -2k_1 V - 2^{\frac{\delta_3+1}{2}} k_2 |V|^{\frac{\delta_3+1}{2}}. \end{aligned} \quad (28)$$

It is affirmed from (28) that the speed error with CFT-SMC will be zero in a finite time (t_f) and the speed trajectory will remain on the sliding surface.

C. Proposed CFT-SMO Design

This section focuses on the estimation of the rotor position from the disturbance (f_e^{dq}) corresponding to the back EMF in (3). The extended state observer for (3) can be designed as follows [29]:

$$\dot{i}_s^{dq} = b_v v_s^{dq} + f_i^{dq} + \hat{f}_e^{dq} + \beta_1^{dq} \varepsilon_i^{dq} \quad (29)$$

$$\dot{\hat{f}}_e^{dq} = \beta_2^{dq} \varepsilon_i^{dq} \quad (30)$$

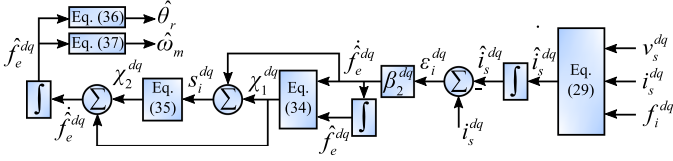


Fig. 4. CFT-SMO structure for PMBLDCM rotor position and speed estimation.

where $[\hat{i}_s^{dq}, \hat{f}_e^{dq}] \rightarrow [i_s^{dq}, f_e^{dq}]$ describes the estimated values of the synthesized phase currents and the total disturbances in the dq -plane. The estimated error of the phase currents can be given as $\varepsilon_i^{dq} = i_s^{dq} - \hat{i}_s^{dq}$. The SMO gains represented as β_1^{dq} and β_2^{dq} are derived from the error dynamics and stability measures. To develop the CFT-SMO for speed estimation, the sliding surface of the CFT (s_i^{dq}) can be derived as follows:

$$s_i^{dq} = -\dot{\hat{f}}_e^{dq} + \mu_1^{dq} \left| \dot{\hat{f}}_e^{dq} \right| \text{sgn} \left(\dot{\hat{f}}_e^{dq} \right) + \mu_2^{dq} \left| \dot{\hat{f}}_e^{dq} \right| \text{sgn} \left(\dot{\hat{f}}_e^{dq} \right) \quad (31)$$

where conditions $\mu_1^{dq}, \mu_2^{dq} > 0$, $0 < \delta_1^{dq}, \delta_2^{dq} < 2$, $\delta_2^{dq} > \delta_1^{dq}$ are satisfied. From the sliding surface error dynamics, s_i^{dq} can also be defined as follows:

$$s_i^{dq} = \int_0^t \left[-k_1^{dq} s_i^{dq} - k_2^{dq} \left| s_i^{dq} \right|^{\delta_3^{dq}} \text{sgn} \left(s_i^{dq} \right) \right] dt \quad (32)$$

where conditions $k_1^{dq}, k_2^{dq} > 0$, $0 < \delta_3^{dq} < 1$ satisfy. To improve the convergence rate against disturbances, the CFT-SMO can be developed by solving (31) and (32) and can be indicated as follows:

$$\hat{f}_e^{dq} = \int_0^t \left[\chi_1^{dq} + \chi_2^{dq} \right] dt \quad (33)$$

$$\chi_1^{dq} = \mu_1^{dq} \left| \dot{\hat{f}}_e^{dq} \right|^{\delta_1^{dq}} \text{sgn} \left(\dot{\hat{f}}_e^{dq} \right) + \mu_2^{dq} \left| \dot{\hat{f}}_e^{dq} \right|^{\delta_2^{dq}} \text{sgn} \left(\dot{\hat{f}}_e^{dq} \right) \quad (34)$$

$$\chi_2^{dq} = \int_0^t \left[k_1^{dq} s_i^{dq} + k_2^{dq} \left| s_i^{dq} \right|^{\delta_3^{dq}} \text{sgn} \left(s_i^{dq} \right) \right] dt. \quad (35)$$

The detailed block diagram approach to estimate \hat{f}_e^{dq} is shown in Fig. 4. It can be seen from [31] that the back-EMF in α -axis is dependent on the rotor electrical angle position. During the transformation of the axes from $\alpha\beta$ -frame to dq -frame using (4), both axes of the EMF in dq -frame contain information of rotor position. Fig. 5 shows such a relationship between the dq -frame EMF and the rotor position $\hat{\theta}_r$. As dq -frame back EMF cannot be estimated directly, the proposed SMC evaluates the disturbance \hat{f}_e^{dq} corresponding to the back EMF. In other words, \hat{f}_e^{dq} has a direct relationship with $\hat{\theta}_r$ as mentioned in the following:

$$\hat{\theta}_r = \tan^{-1} \left(\hat{f}_e^q / \hat{f}_e^d \right). \quad (36)$$

Again, the rotor speed of PMBLDCM can be estimated in the following, which provides the minimum tracking error for utilization in the FOC system:

$$\hat{\omega}_m = \frac{\left(\hat{f}_e^q s_i^d - \hat{f}_e^d s_i^q \right)}{p \left\| \hat{f}_e^{dq} \right\|^2} \quad (37)$$

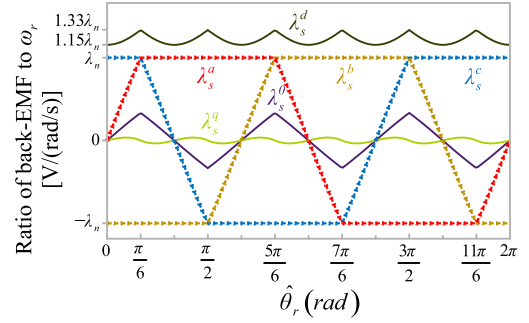


Fig. 5. Back-EMF relationship with $\hat{\theta}_r$.

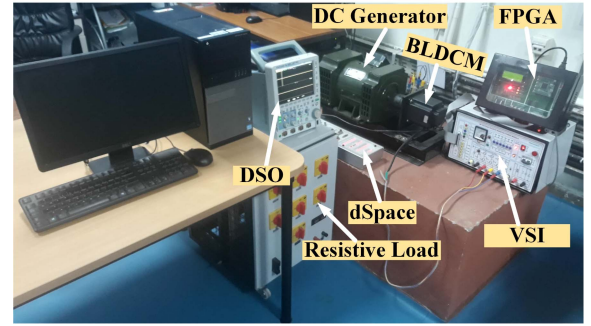


Fig. 6. PMBLDCM hardware prototype.

where p is the number of pole pairs of PMBLDCM and $\|\hat{f}_e^{dq}\|$ denotes the norm of \hat{f}_e^{dq} . It is obvious that if the injection of the sliding surface output s_i^{dq} is continuous, the estimated speed can be smooth. Otherwise, if there is chattering in s_i^{dq} , the output injections contain high-frequency noise and cannot even be used in the PMBLDCM FOC system. The block diagram algorithm of the speed/flux observer proposed in this article based on CFT-SMO is shown in Fig. 4.

IV. RESULTS AND DISCUSSIONS

In this section, the feasibility study of the proposed CFT-SMC estimation techniques with the FOC scheme is carried out by experimental verification. The experimental prototype consists of a 2.5-kW PMBLDCM, a dc generator, and a three-phase 2L-VSI with a battery pack, as shown in Fig. 6. The shaft of PMBLDCM is coupled to a dc generator that is considered a load. The specifications of the PMBLDCM drive are given in Table I. Initially, the PMBLDCM drive control is simulated in MATLAB/Simulink. With satisfactory simulation performance, PWM signals are generated by implementing the proposed control strategy on a dSPACE (DS1104) controller. During the execution process in DS1104, a sample period of 50 μ s is maintained for the proposed control action. DS1104 has integrated analog-to-digital (ADC) and digital-to-analog (DAC) units. ADCs are particularly utilized to process measured current and voltage signals, whereas DACs are used to record the performance results of the overall drive through a digital storage oscilloscope. To evaluate the proposed control strategies, several test scenarios are examined as mentioned in the following.

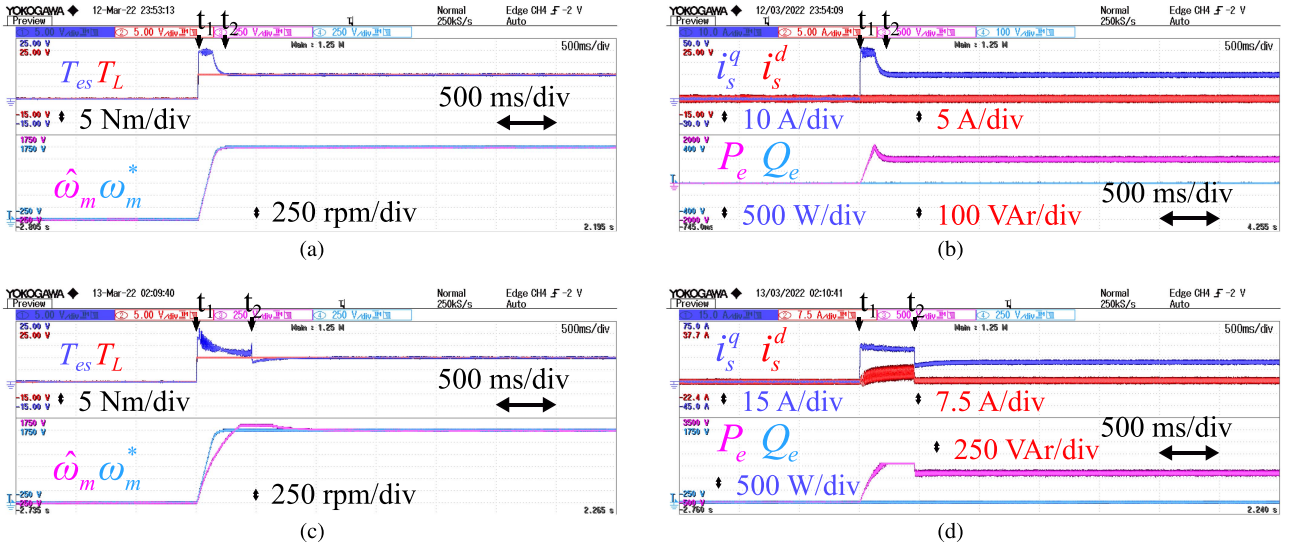


Fig. 7. Experimental results: CFT-SMC-based PMBLDCM drive performance considering Scenario-1. (a) Waveforms of T_{es} and $\hat{\omega}_m$ with proposed controller. (b) Waveforms of i_s^q , i_s^d , P_e , and Q_e with proposed controller. (c) Waveforms T_{es} and $\hat{\omega}_m$ for comparison study [32]. (d) Waveforms of i_s^q , i_s^d , P_e , and Q_e for comparison study [32].

TABLE I
PMBLDCM DRIVE SPECIFICATIONS

Simulation and hardware PMBLDCM parameters	
3Φ , 8 Pole, $V_{dc}=240$ V, $P_{rated}=2.5$ kW, $\omega_{rated}=1500$ r/min,	
$T_{rated}=20$ N.m, $\lambda_n=0.175$ V.s/rad, $R_s=2.4$ Ω ,	
$L_s=8.5$ mH, $J=0.089$ kg.m ² , $B=10^{-3}$ kg/s.	
Simulation and hardware controller parameters	
Sample time (simulation), $T_s=10$ μ s, Sample time (Experiment),	
$T_s=50$ μ s, Switching Frequency, $f_{sw}=5$ kHz,	
Dead time, $t_d=1$ μ s, $k_1=1.5$, $k_p^d=95$, $k_p^q=115$	
$k_2=1.5$, $k_i^d=1500$, $k_i^q=1500$	

Scenario 1: Change in $T_L = 0 \rightarrow T_L = 10$ N · m with a step command from $\omega_m^* = 0$ to 1500 r/min.

Scenario 2: Change in $T_L = 10 \rightarrow T_L = -10$ N · m with the step command of $\omega_m^* = 0 \rightarrow 300 \rightarrow 600 \rightarrow -300 \rightarrow 0$ r/min.

Scenario 3: Change in $T_L = 5 \rightarrow 10 \rightarrow 5$ N · m with a steady-state speed command of $\omega_m^* = 1500$ r/min.

A. Scenario 1: Rated Speed Performance

In this section, the steady-state operation of PMBLDCM is discussed and compared with that of the approach given in [32]. Torque and current performance is evaluated with the goal of reducing related ripples. The impact of disturbances that include iron loss acting on the drive system has been investigated and compared. It is worth mentioning that existing approaches have not considered iron losses in the SMO to improve the performance of PMBLDCM. The developed motor torque (T_{es}) with load torque (T_L), estimated motor speed ($\hat{\omega}_m$) with reference speed command (ω_m^*), stator currents (i_s^{dq}) in dq -frame and active power (P_e) with reactive power (Q_e) for the proposed CFT-SMC technique are shown in Fig. 7(a) and (b) during Scenario 1, respectively. The comparative study with Scenario 1 is shown in Fig. 7(c) and (d). Here, a step change in $\hat{\omega}_m$ from

TABLE II

RIPPLE % COMPARISON FOR PROPOSED CFT-SMO AND SMO-[32] DURING (I) SCENARIO 1 (S-1), (II) SCENARIO 2 (S-2) AND (III) SCENARIO 3 (S-3)

Parameters (in %)	Proposed			SMO-[32]			% Improvement		
	S-1	S-2	S-3	S-1	S-2	S-3	S-1	S-2	S-3
ΔT_{es}	2.3	3.2	2.3	3.2	4.15	3.35	28.1	22.8	31.3
$\Delta \hat{\omega}_m$	2.2	4.1	7.2	4.1	7.9	11.7	46.3	48.1	38.4
ΔI_s^{dq}	3.3	7.2	5.1	8.3	9.1	7.9	60.0	42.8	35.1
ΔP	1.3	2.2	2.6	2.7	4.9	8.1	51.8	55.1	67.9
Δi_{bat}	6.8	8.6	10.3	7.9	10.7	13.9	13.9	19.6	25.8
η	93.5	86	92	87	77.5	88.2	6.9	9.8	4.1

0 to 1500 r/min with $T_L = 10$ N · m is given in t_1 s. The drive system takes 0.175 and 0.275 s with the proposed CFT-SMC and [32], respectively, to reach steady-state condition. In addition to this, another benefit of the proposed method can be evaluated in terms of reduced ripple content in the T_{es} , $\hat{\omega}_m$, i_s^q , profile of PMBLDCM from Fig. 7. The steady-state ripple improvement in T_{es} and $\hat{\omega}_m$ is found to be 52.02% and 42%, respectively, for Scenario 1. It can be concluded from Fig. 7(b) that P_e demand matches the dynamics of T_{es} , and the nearly zero Q_e shows reduced losses with perfect synchronization. However, such achievements have not been noted in [32], as shown in Fig. 7(d). i_s^d is always kept at zero with CFT-SMC, whereas i_s^d reaches 9.3 A during the transition region and 5.6 A in the steady-state region with [32]. The battery current (i_{bat}) and the three-phase stator currents i_s^{abc} for the proposed method and the method presented in [32] are shown in Fig. 8(a) and (c), respectively. These plots show less ripple for the proposed CFT-SMC method. Synthesized phase currents $i_s^{\alpha\beta}$ and phase back-EMF $e_s^{\alpha\beta}$ are shown in Fig. 8(b). The trajectory plots of $i_s^{\alpha\beta}$ and $e_s^{\alpha\beta}$ are shown in Fig. 8(b) to guarantee the efficacy of the proposed method. For comparison study, $i_s^{\alpha\beta}$ and $e_s^{\alpha\beta}$ with their trajectory plot can be shown in Fig. 8(d). Figs. 7 and 8 are given in Table II for Scenario 1. It reports a numerical comparison of the improvement % in the ripple content of T_{es} , ω_m , P_e , I_s^{dq} , and

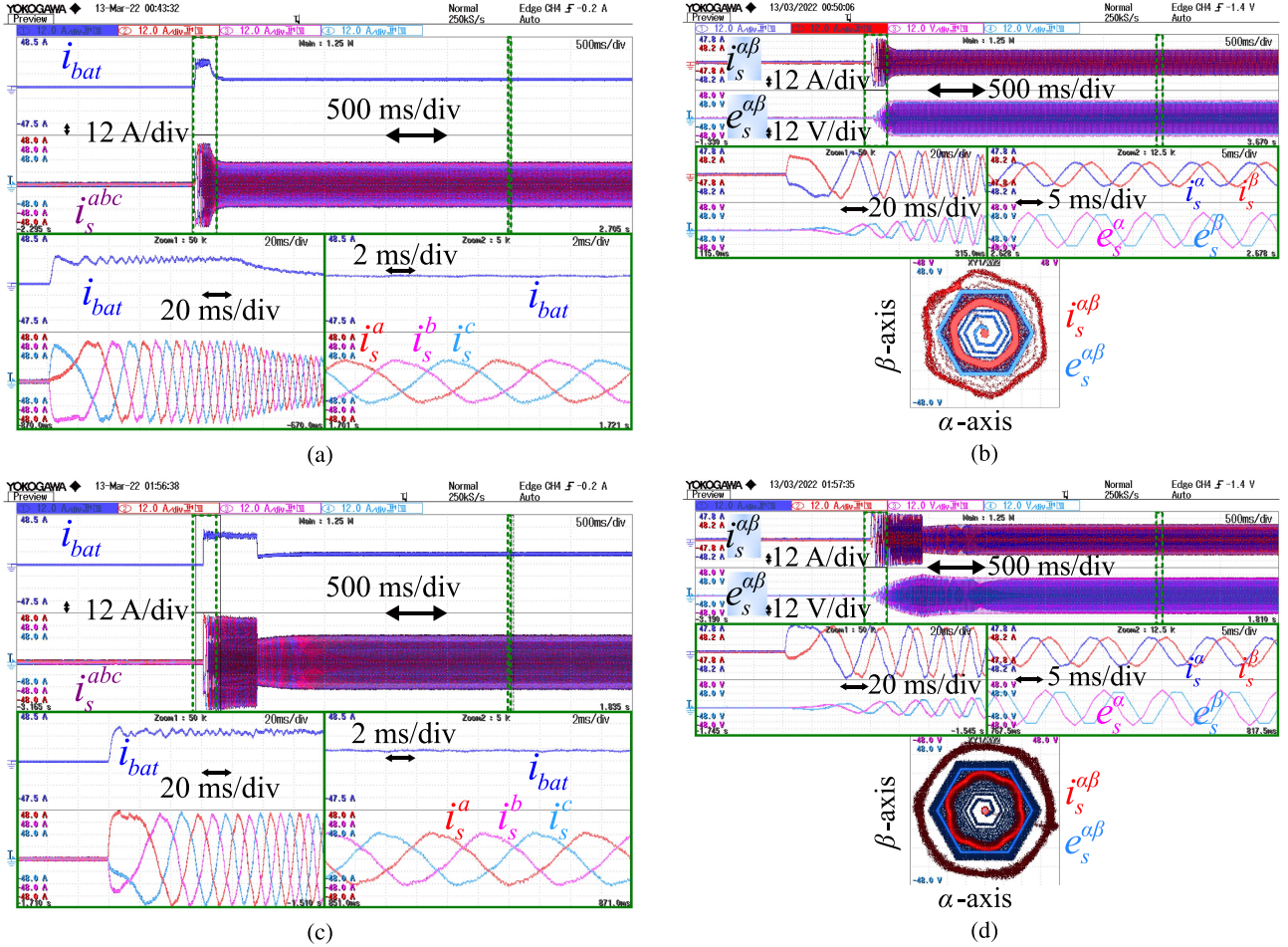


Fig. 8. Experimental results: Battery and drive current performance during Scenario-1. (a) Waveforms of i_{bat} and i_s^{abc} with proposed controller. (b) Waveforms and trajectory plot of $i_s^{\alpha\beta}$ and $e_s^{\alpha\beta}$ with proposed controller. (c) Waveforms of i_{bat} and i_s^{abc} for comparison study [32]. (d) Waveforms and trajectory plot of $i_s^{\alpha\beta}$ and $e_s^{\alpha\beta}$ for comparison study [32].

I_{bat} between the proposed CFT-SMC and the approach described in [32]. To achieve torque ripple suppression during Scenario 1, the proposed CFT-SMC provides better performance when the motor is operating in a steady state. In addition, the proposed CFT-SMC provides better current ripple and speed tracking.

B. Scenario 2: Speed Reversal and Low Speed Performance

The performance of PMSBLDCM is also tested and compared during low-speed and speed reversal conditions. In Scenario 2, a variable load with $T_L = 10 \rightarrow -10 \text{ N} \cdot \text{m}$ is considered for the operation of the PMSBLDCM drive. Initially, ω^* changes from 0 to 300 r/min in t_1 s and gradually settles within 30 ms, as shown in Fig. 9(a). Again, at t_2 s, a speed command of 600 r/min is set, which settles at a rate of 10000 rpm/s. Furthermore, ω^* changes to -300 r/min and then reaches 0 r/min at t_3 s and t_4 s, respectively. The overall comparative study of the speed reversal performance of PMSBLDCM drives can be shown in Fig. 9(c) and (d). The SMO with [32] has a high torque and current ripple throughout the speed range, whereas the proposed CFT-SMC tracks the rotor speed very precisely with minimal tracking error. It can also be observed that the proposed CFT-SMC can estimate

the rotor speed during low-speed operation, as well as the speed reversal period. PMSBLDCM has significant torque ripple and spikes at high speeds, causing the speed and current waveforms to be distorted, leading to weak drive performance with [32]. However, the CFT-SMC guarantees better improvement in terms of ripples and improves the drive profile at a higher speed. Once the speed is reduced to -300 r/min, the ripple of the electromagnetic torque steadily increases, resulting in a large current ripple, as can be compared with Fig. 9(b) and (d). The proposed method proves the improved torque and current ripple under wide-speed operation. The experimental findings of i_s^d , i_s^q , P_e , and Q_e are shown in Fig. 11(b). Regenerative action can be seen from P_e during the speed reversal operation at t_3 s. The same performance can also be observed from the battery current in Fig. 11(a). Here, the phase currents clearly indicate the petal wave patterns. Using Scenario 2 in Table II, it can be seen that the magnitude of the ripple contents of T_{es} , ω_m , P_e , I_s^{dq} , and I_{bat} has been improved with the proposed method. With [32], the torque ripple is higher considering the iron loss. It is worth noting that the proposed CFT-SMC yields an appreciable reduction of the torque ripple at wide range of speed operation.

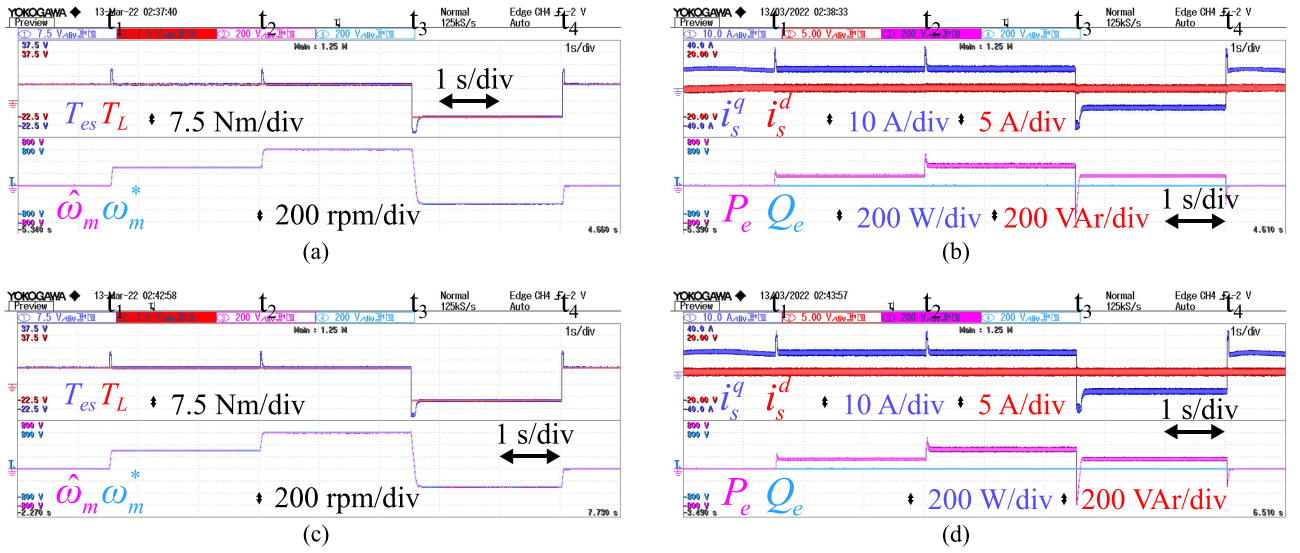


Fig. 9. Experimental results: CFT-SMC-based PMLBDCM drive performance considering Scenario-2. (a) Waveforms of T_{es} and $\hat{\omega}_m$ with proposed controller. (b) Waveforms of i_s^q , i_s^d , P_e , and Q_e with proposed controller. (c) Waveforms of T_{es} and $\hat{\omega}_m$ for comparison study [32]. (d) Waveforms of i_s^q , i_s^d , P_e , and Q_e for comparison study [32].

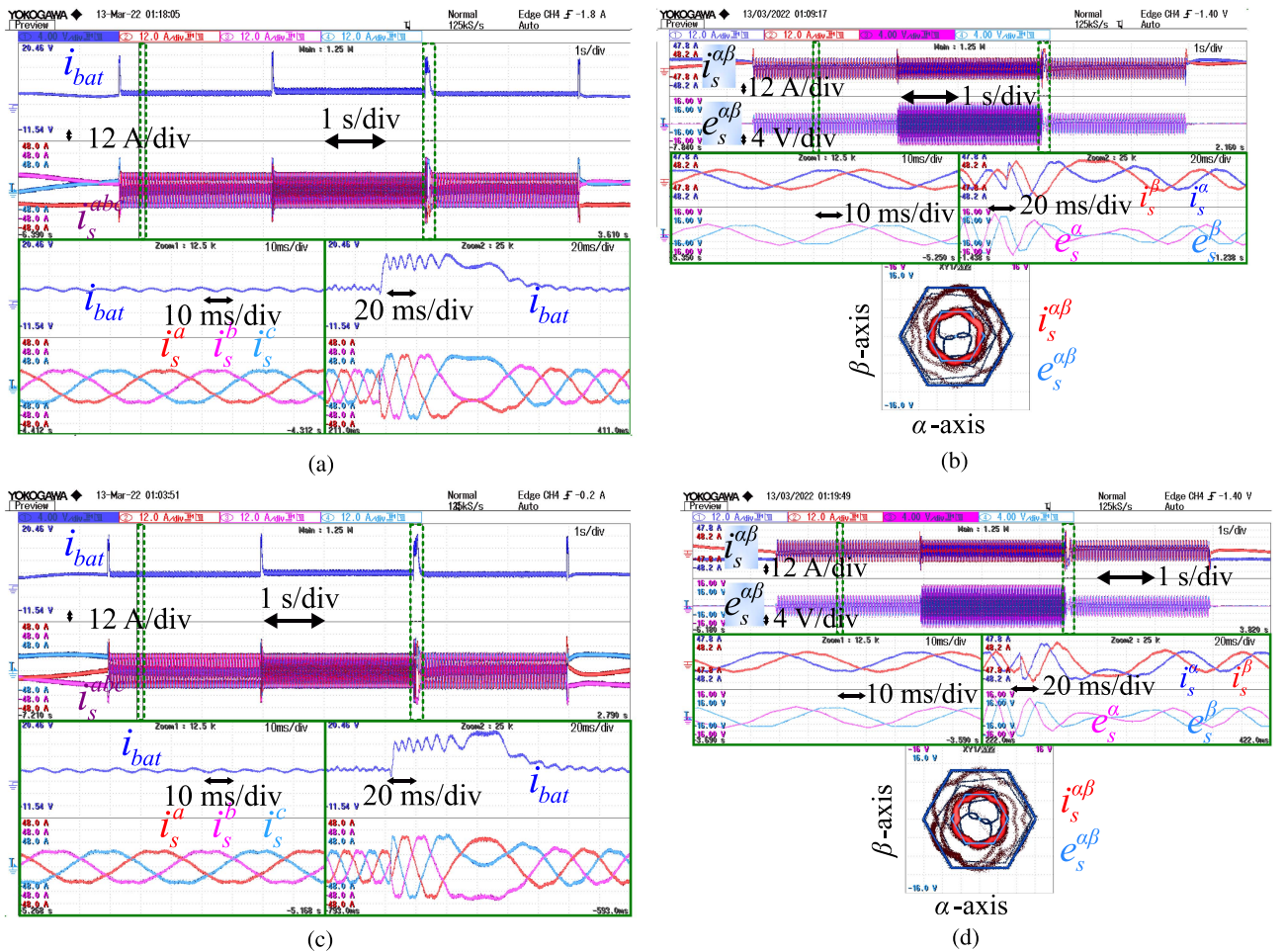


Fig. 10. Experimental results: battery and drive current performance during Scenario-2. (a) Waveforms of i_{bat} and i_s^{abc} with proposed controller. (b) Waveforms and trajectory plot of $i_s^{\alpha\beta}$ and $e_s^{\alpha\beta}$ with proposed controller. (c) Waveforms of i_{bat} and i_s^{abc} for comparison study [32]. (d) Waveforms and trajectory plot of $i_s^{\alpha\beta}$ and $e_s^{\alpha\beta}$ for comparison study [32].

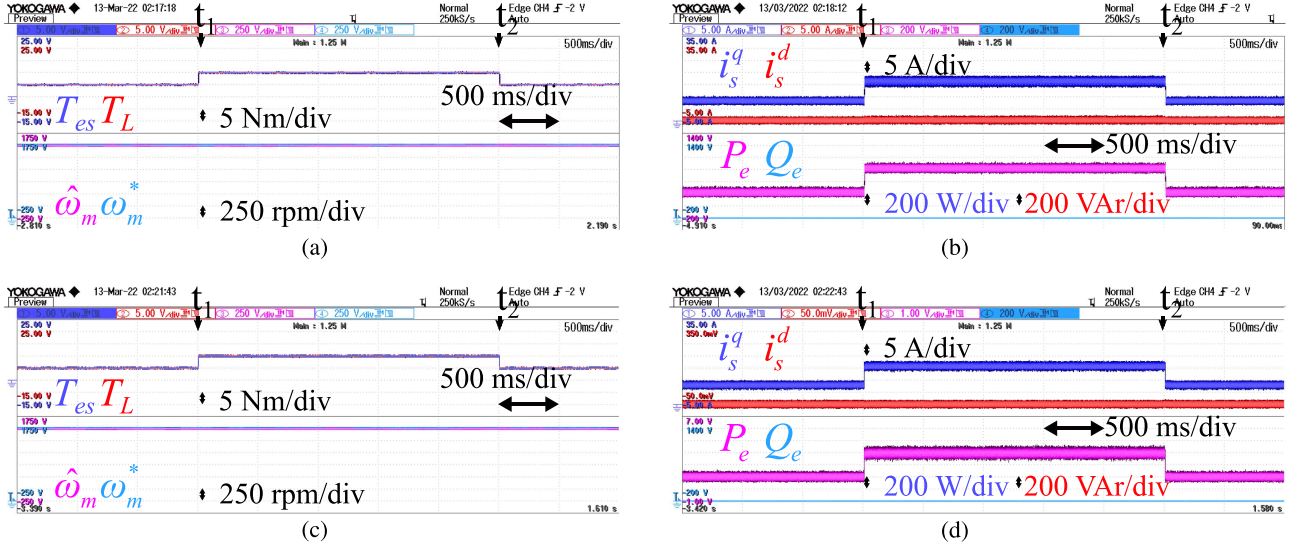


Fig. 11. Experimental results: CFT-SMC-based PMBLDCM drive performance considering Scenario-3. (a) Waveforms of T_{es} and $\hat{\omega}_m$ with proposed controller. (b) Waveforms of i_s^q , i_s^d , P_e , and Q_e with proposed controller. (c) Waveforms of T_{es} and $\hat{\omega}_m$ for comparison study [32]. (d) Waveforms of i_s^q , i_s^d , P_e , and Q_e for comparison study [32].

C. Scenario 3: Load Change Performance

The steady-state performance of the PMBLDCM drives at $\omega_m^* = 1500$ r/min can be seen in Figs. 11 and 12. It can be observed from Fig. 11(a) that $\hat{\omega}_m$ is closely tracking $\hat{\omega}_m^*$. At t_1 s, a load of $T_L = 5$ N · m is applied to the PMBLDCM drive system. It can be seen that T_{es} can track T_L very accurately. However, torque performance with the FOC method in [32] is observed with a significant deviation from its reference value, as seen from the comparative results shown in Fig. 11(c). The ripple improvement in T_{es} and $\hat{\omega}_m$ with the proposed CFT-SMC is concluded to be 53.1% and 41.1%, respectively. The experimental findings of i_s^q , i_s^d , P_e , and Q_e are shown in Fig. 11(b), and their comparative performance is shown in Fig. 11(d). The steady-state performance of i_{bat} and i_s^{abc} at $T_L = 5$, 10, and 5 N · m with step command of $\omega_m^* = 1500$ r/min is shown in Fig. 12(a). Their performance can be assessed with the comparative results provided in Fig. 12(c). The plots of $i_s^{\alpha\beta}$ and $e_s^{\alpha\beta}$ with $T_L = 5 \rightarrow 10 \rightarrow 5$ N · m with constant speed command of $\omega_m^* = 1500$ r/min with the proposed method and the comparative method from [32] are shown in Fig. 12(b) and (d), respectively. It has been noted that the trajectory appears like a petal structure and is in line with the theoretical assumptions on reduced ripple contents. In Scenario 3, the torque ripple is more prominent (nearly twice) for [32] compared with the proposed CFT-SMC, as given in Table II and Figs. 11 and 12. Moreover, the proposed CFT-SMC is effective in suppressing the ripple content in the PMBLDCM drives performance.

D. Transient Performance

With the proposed controller, the robustness and fast dynamic characteristics of the PMBLDCM drive are evaluated during transient conditions. During the speed transition, the change in load torque and disturbances caused by variation of the parameters, the overall drive may be subjected to transient conditions. To determine whether the proposed controller is

effective, current and torque ripples are used as measures of performance evaluation. The plot of the waveforms of each estimated quantity against its reference value distinguishes the speed at which the FOC settles the desired performance. This performance evaluation can be observed from Figs. 7, 9, and 11. The fast Fourier transform (FFT) analysis of the phase-a stator current is characterized, which has a THD of 5.83% due to its pattern of petal wave current. This THD level of the stator phase current is significantly lower than that of the conventional quasi-square wave pattern. The analysis of the motor torque harmonics reveals a THD of 2.39%, in which the sixth and twelfth harmonics dominate with magnitudes of 2.3% and 0.1%, respectively.

E. Parameter Variation and Comparative Performance

Since the CFT-SMO is dependent on electrical parameters, variations in the parameters can significantly affect the estimated motor speed. It should be noted that the estimation of motor speed is more specifically based on the disturbance associated with the back-EMF (\hat{f}_e^{dq}), which has all the disturbance associated with the variations of the parameters. Speed tracking performance under steady-state and transient conditions is tested for Scenario 3 under parameter variation, as shown in Fig. 13. Taking into account an uncertain disturbance changing from 0.233 to 0.405 per unit at $t = t_1$ s, the speed estimation with the tracking error (ϵ_ω) is shown in Fig. 13(a) with the proposed CFT-SMC and in Fig. 13(b) with SMO-[32]. The minimal speed tracking error of 5 r/min is observed with the proposed CFT-SMC. However, $\hat{\omega}_m$ decreases by 30 r/min after T_L increases to the rated value with SMO-[32]. It can be well observed that the proposed CFT-SMO performs much better than SMO-[32] in terms of disturbance estimation and speed tracking precision. Furthermore, the CFT-SMC and the existing SMC require 80 and 110 ms, respectively, to restore the nominal speed. When the speed

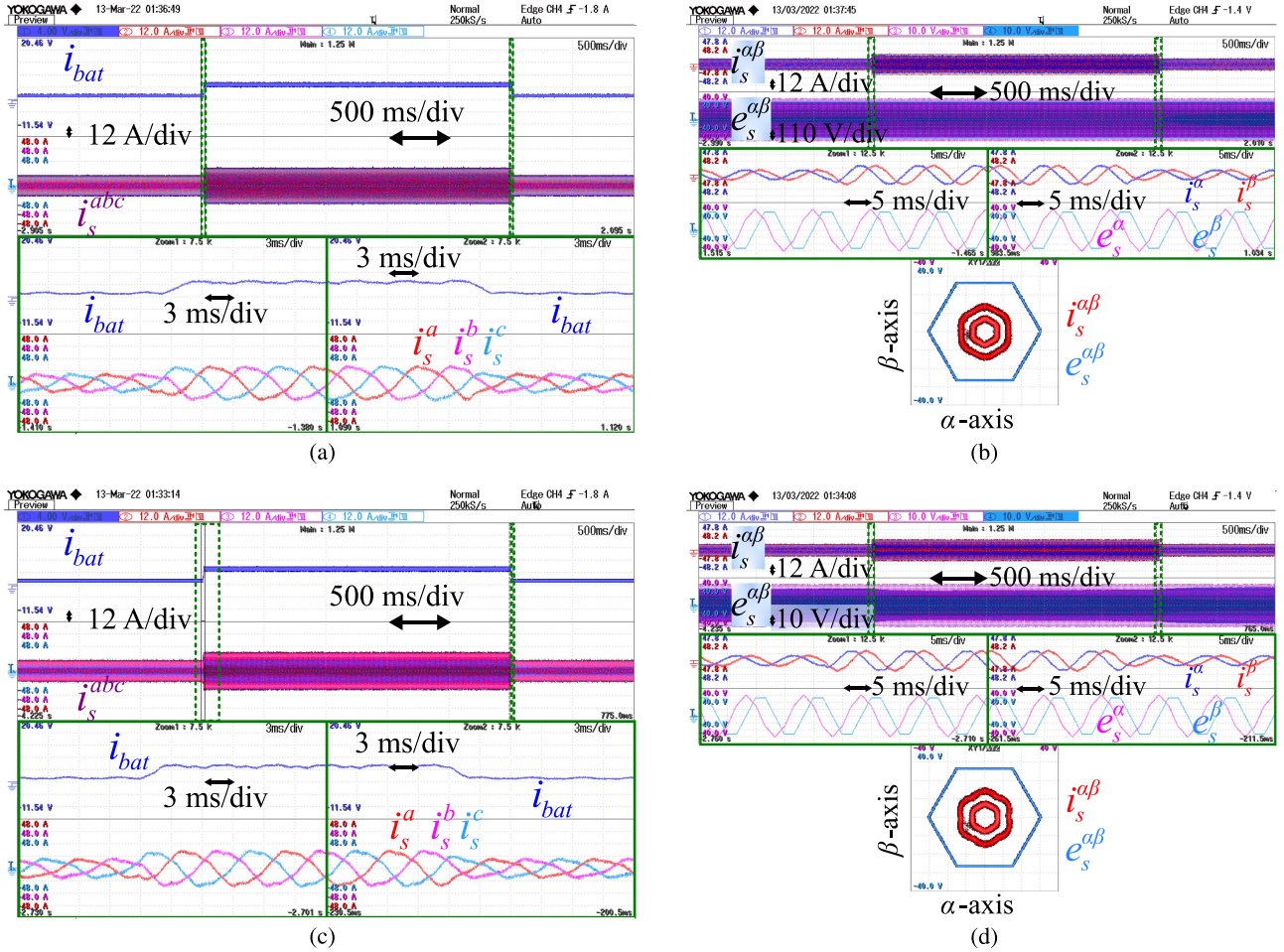


Fig. 12. Experimental results: Battery and drive current performance during Scenario-3. (a) Waveforms of i_{bat} and i_s^{abc} with proposed controller. (b) Waveforms and trajectory plot of $i_s^{\alpha\beta}$ and $e_s^{\alpha\beta}$ with proposed controller. (c) Waveforms of i_{bat} and i_s^{abc} for comparison study [32]. (d) Waveforms and trajectory plot of $i_s^{\alpha\beta}$ and $e_s^{\alpha\beta}$ for comparison study [32].

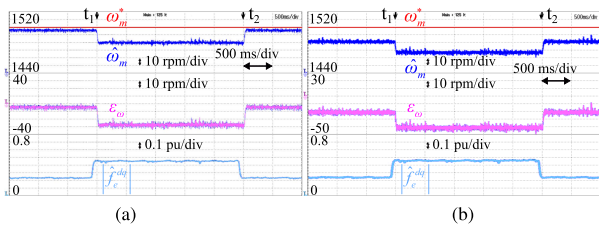


Fig. 13. Hardware results: Tracking error of the $\hat{\omega}_m$ at $\omega_m = 1500$ r/min with change in T_L considering Scenario 3. (a) With proposed CFT-SMO. (b) With SMO-[32].

drop and recovery period are compared, the proposed method outperforms SMO-[32] in terms of disturbance rejection.

For a better comparative evaluation, an experimental validation is performed between the proposed controller, SMO-[32], and MTPA-DTC-[26], as shown in Fig. 14. Fig. 14(a) shows the %THD of the stator phase current (i_s^a) with respect to the speed ratio k_ω ($= \hat{\omega}_m/\omega_n$, ω_n is the nominal motor angular speed), whereas Fig. 14(b) represents the torque ripple (ΔT_{es}) and the efficiency (η) profiles of PMBLDCM with respect to k_ω .

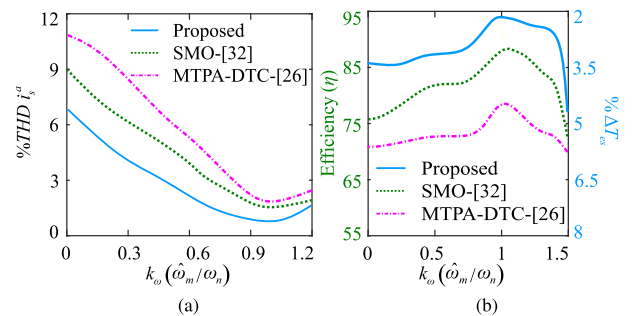


Fig. 14. Comparative validation study between proposed controller, SMO-[32] and MTPA-DTC-[26]. (a) % THD performance analysis. (b) % ΔT_e and efficiency analysis.

This comparative study validates the superiority of the proposed controller over the existing control strategies SMO-[32] and MTPA-DTC-[26]. At $k_\omega = 0$, the % ΔT_{es} for the proposed SMO, SMO-[32], and MTPA-DTC-[26] are recorded as 3.35%, 4.95% and 5.65%, respectively. The efficiencies (η) of 86, 76, and 71 units are observed for the proposed observer, SMO-[32], and

MTPA-DTC-[26], respectively. With the increase in speed for $k_{\omega} = 1$, i.e., at rated speed, $\% \Delta T_{es}$ is observed to be much reduced and η much improved compared with SMO-[32] and MTPA-DTC-[26]. Furthermore, with an increase in speed for $k_{\omega} > 1$, again the PMBLDCM achieves a better torque ripple and higher efficiency with the proposed SMO.

V. CONCLUSION

An approach to estimate the speed of PMBLDCM drives with iron loss based on CFT-SMO was proposed. It was possible to observe the rotor position signals more accurately and efficiently without using any sensors. In the proposed approach, an estimate of the total disturbance was incorporated, reducing the complexity of designing and executing higher order models. Taking into account the unknown disturbances, a CFT-SMC-based speed controller was provided that offered improved speed tracking. In addition, the FOC gave an accurate current control that matches the back-EMF when it used optimal modulation of the VSI drive. In addition to minimizing copper loss and optimizing drive efficiency, iron loss was also used to influence FOC. Laboratory testing showed that drive performance was improved when the suggested technique was used. A petalwave Lissajous pattern was observed in the motor currents of the stationary reference frame, ensuring less ripple, lower copper losses, and smoother motor torque. Based on the comparisons, it seemed that the proposed algorithm performed better than the existing ones. In addition to high-performance applications, such as electric vehicles, the suggested sensorless PMBLDCM algorithm could also be used in the case of low power consumption. Further application of the aforementioned method to enhance the performance of electric cars will involve extending the aforementioned method to field weakening and regenerative braking applications, with an emphasis on regenerative braking.

V. ACKNOWLEDGMENT

The authors would like to thank S. Prakash, a Ph.D. scholar at IIT Patna, for his assistance during the collection of experimental data.

REFERENCES

- [1] M. Ebadpour, N. Amiri, and J. Jatskevich, "Fast fault-tolerant control for improved dynamic performance of hall-sensor-controlled brushless DC motor drives," *IEEE Trans. Power Electron.*, vol. 36, no. 12, pp. 14051–14061, Dec. 2021.
- [2] H. Jin, G. Liu, and S. Zheng, "Commutation error closed-loop correction method for sensorless BLDC motor using hardware-based floating phase back-EMF integration," *IEEE Trans. Ind. Informat.*, vol. 18, no. 6, pp. 3978–3986, Jun. 2022.
- [3] A. Damiano, A. Floris, G. Fois, I. Marongiu, M. Porru, and A. Serpi, "Design of a high-speed ferrite-based brushless DC machine for electric vehicles," *IEEE Trans. Ind. Appl.*, vol. 53, no. 5, pp. 4279–4287, Sep./Oct. 2017.
- [4] J. Zhang, Y. Xia, Z. Zhang, and X. Chen, "Influence of driving mode on loss characteristics of doubly salient brushless motor with rectangular wire armature winding," *IEEE Trans. Magn.*, vol. 58, no. 2, pp. 1–6, Feb. 2022.
- [5] M. Fasil, N. Mijatovic, B. B. Jensen, and J. Holboll, "Nonlinear dynamic model of PMBLDC motor considering core losses," *IEEE Trans. Ind. Electron.*, vol. 64, no. 12, pp. 9282–9290, Dec. 2017.
- [6] H. Jin, G. Liu, H. Li, B. Chen, and H. Zhang, "A fast commutation error correction method for sensorless BLDC motor considering rapidly varying rotor speed," *IEEE Trans. Ind. Electron.*, vol. 69, no. 4, pp. 3938–3947, Apr. 2022.
- [7] H. Zhang, M. Dou, and L. Yan, "Effects of stator iron loss and current-loop delay on copper-loss-minimizing torque control of BLDCM: Analysis and improvements," *IEEE Trans. Power Electron.*, vol. 34, no. 6, pp. 5620–5631, Jun. 2019.
- [8] J. Park and D.-H. Lee, "Simple commutation torque ripple reduction using PWM with compensation voltage," *IEEE Trans. Ind. Appl.*, vol. 56, no. 3, pp. 2654–2662, May/Jun. 2020.
- [9] L. Yang, Z. Q. Zhu, H. Bin, Z. Zhang, and L. Gong, "Virtual third harmonic back EMF-based sensorless drive for high-speed BLDC motors considering machine parameter asymmetries," *IEEE Trans. Ind. Appl.*, vol. 57, no. 1, pp. 306–315, Jan./Feb. 2021.
- [10] S. B. Santra, A. Chatterjee, D. Chatterjee, S. Padmanaban, and K. Bhattacharya, "High efficiency operation of brushless DC motor drive using optimized harmonic minimization based switching technique," *IEEE Trans. Ind. Appl.*, vol. 58, no. 2, pp. 2122–2133, Mar./Apr. 2022.
- [11] X. Zhang, Y. Wang, G. Liu, and X. Yuan, "Robust regenerative charging mode control based on T-S fuzzy sliding-mode approach for advanced electric vehicle," *IEEE Trans. Transport. Electrification.*, vol. 2, no. 1, pp. 52–65, Mar. 2016.
- [12] D. Zhang, G. Liu, H. Zhou, and W. Zhao, "Adaptive sliding mode fault-tolerant coordination control for four-wheel independently driven electric vehicles," *IEEE Trans. Ind. Electron.*, vol. 65, no. 11, pp. 9090–9100, Nov. 2018.
- [13] Y.-C. Liu, S. Laghrouche, D. Depernet, A. Djerdir, and M. Cirrincione, "Disturbance-observer-based complementary sliding-mode speed control for PMSM drives: A super-twisting sliding-mode observer-based approach," *IEEE Trans. Emerg. Sel. Topics Power Electron.*, vol. 9, no. 5, pp. 5416–5428, Oct. 2021.
- [14] H. Sheh Zad, T. I. Khan, and I. Lazoglu, "Design and adaptive sliding-mode control of hybrid magnetic bearings," *IEEE Trans. Ind. Electron.*, vol. 65, no. 3, pp. 2537–2547, Mar. 2018.
- [15] U. K. Kalla, B. Singh, S. S. Murthy, C. Jain, and K. Kant, "Adaptive sliding mode control of standalone single-phase microgrid using hydro, wind, and solar PV array-based generation," *IEEE Trans. Smart Grid.*, vol. 9, no. 6, pp. 6806–6814, Nov. 2018.
- [16] B. Tang, W. Lu, B. Yan, K. Lu, J. Feng, and L. Guo, "A novel position speed integrated sliding mode variable structure controller for position control of PMSM," *IEEE Trans. Ind. Electron.*, vol. 69, no. 12, pp. 12621–12631, Dec. 2022.
- [17] C.-W. Hung, C.-T. Lin, C.-W. Liu, and J.-Y. Yen, "A variable-sampling controller for brushless DC motor drives with low-resolution position sensors," *IEEE Trans. Ind. Electron.*, vol. 54, no. 5, pp. 2846–2852, Oct. 2007.
- [18] X. Peng, M. Jia, L. He, X. Yu, and Y. Lv, "Fuzzy sliding mode control based on longitudinal force estimation for electro-mechanical braking systems using BLDC motor," *CES Trans. Elect. Machines Syst.*, vol. 2, no. 1, pp. 142–151, Mar. 2018.
- [19] S. G. Malla et al., "Whale optimization algorithm for PV based water pumping system driven by BLDC motor using sliding mode controller," *IEEE Trans. Emerg. Sel. Topics Power Electron.*, vol. 10, no. 4, pp. 4832–4844, Aug. 2022.
- [20] B. Xu, L. Zhang, and W. Ji, "Improved non-singular fast terminal sliding mode control with disturbance observer for PMSM drives," *IEEE Trans. Transport. Electrification.*, vol. 7, no. 4, pp. 2753–2762, Dec. 2021.
- [21] H. Wang et al., "Continuous fast nonsingular terminal sliding mode control of automotive electronic throttle systems using finite-time exact observer," *IEEE Trans. Ind. Electron.*, vol. 65, no. 9, pp. 7160–7172, Sep. 2018.
- [22] Y. Wang, X. Zhang, X. Yuan, and G. Liu, "Position-sensorless hybrid sliding-mode control of electric vehicles with brushless DC motor," *IEEE Trans. Veh. Technol.*, vol. 60, no. 2, pp. 421–432, Feb. 2011.
- [23] A. K. Junejo, W. Xu, C. Mu, and Y. Liu, "Improved continuous fast terminal sliding mode control for speed regulation of surface-mounted permanent magnet synchronous motor," in *Proc. IEEE 21st Int. Conf. Elect. Machines Syst.*, 2018, pp. 93–98.
- [24] M. Zhou, S. Cheng, Y. Feng, W. Xu, L. Wang, and W. Cai, "Full-order terminal sliding-mode-based sensorless control of induction motor with gain adaptation," *IEEE Trans. Emerg. Sel. Topics Power Electron.*, vol. 10, no. 2, pp. 1978–1991, Apr. 2022.
- [25] A. Bosso, C. Conficoni, D. Raggini, and A. Tilli, "A computational-effective field-oriented control strategy for accurate and efficient electric propulsion of unmanned aerial vehicles," *IEEE/ASME Trans. Mechatronics*, vol. 26, no. 3, pp. 1501–1511, Jun. 2021.
- [26] A. Khazaei, H. A. Zarchi, G. A. Markadeh, and H. Mosaddegh Hesar, "MTPA strategy for direct torque control of brushless DC motor drive," *IEEE Trans. Ind. Electron.*, vol. 68, no. 8, pp. 6692–6700, Aug. 2021.
- [27] K. Xia, Y. Ye, J. Ni, Y. Wang, and P. Xu, "Model predictive control method of torque ripple reduction for BLDC motor," *IEEE Trans. Magn.*, vol. 56, no. 1, pp. 1–6, Jan. 2020.

- [28] A. G. de Castro, W. C. A. Pereira, T. E. P. de Almeida, C. M. R. de Oliveira, J. Roberto Boffino de Almeida Monteiro, and A. A. de Oliveira, "Improved finite control-set model-based direct power control of BLDC motor with reduced torque ripple," *IEEE Trans. Ind. Appl.*, vol. 54, no. 5, pp. 4476–4484, Sep./Oct. 2018.
- [29] P. Kumar, A. R. Beig, D. V. Bhaskar, K. A. Jaafari, U. R. Muduli, and R. K. Behera, "An enhanced linear active disturbance rejection controller for high performance PMSBLDCM drive considering iron loss," *IEEE Trans. Power Electron.*, vol. 36, no. 12, pp. 14087–14097, Dec. 2021.
- [30] U. R. Muduli, A. R. Beig, R. K. Behera, K. A. Jaafari, and J. Y. Alsawalhi, "Predictive control with battery power sharing scheme for dual open-end-winding induction motor based four-wheel drive electric vehicle," *IEEE Trans. Ind. Electron.*, vol. 69, no. 6, pp. 5557–5568, Jun. 2022.
- [31] G. Buja, M. Bertoluzzo, and R. K. Keshri, "Torque ripple-free operation of PM BLDC drives with petal-wave current supply," *IEEE Trans. Ind. Electron.*, vol. 62, no. 7, pp. 4034–4043, Jul. 2015.
- [32] L. Qu, W. Qiao, and L. Qu, "An extended-state-observer-based sliding-mode speed control for permanent-magnet synchronous motors," *IEEE Trans. Emerg. Sel. Topics Power Electron.*, vol. 9, no. 2, pp. 1605–1613, Apr. 2021.



Prashant Kumar (Member, IEEE) received the B.Tech. degree in electrical and electronics engineering from the Guru Ramdas Khalsa Institute of Science and Technology Jabalpur, India, in 2012, and the M.Tech. degree in electrical engineering in 2018 from the Indian Institute of Technology, (Indian School of Mines) Dhanbad, India, where he is currently working toward Ph.D. degree in electrical engineering.

He was a Visiting Scholar with the Department of Electrical Engineering and Computer Science, Khalifa University, Abu Dhabi, UAE in 2020. His research interests include PM BLDC motor drives and its control.



Devara Vijaya Bhaskar (Senior Member, IEEE) received the B.Tech degree in electrical and electronics engineering from Jawaharlal Nehru Technological University, Hyderabad, India in 2006, and the M.Tech and Ph.D. degrees in electrical engineering from the National Institute of Technology Warangal, Telangana, India, in 2009 and 2017, respectively.

He is currently an Assistant Professor with the Department of Electrical Engineering, Indian Institute of Technology (Indian School of Mines), Dhanbad, Jharkhand, India. His research interests include low cost drive converters for electric vehicle and household appliances, and nonlinear control.



Ranjan Kumar Behera (Senior Member, IEEE) received the B.Eng. degree in electrical engineering from the Regional Engineering College Rourkela, Rourkela, India, in 1998, and the M.Tech. and Ph.D. degrees in electrical engineering from the Indian Institute of Technology Kanpur, Kanpur, India, in 2003 and 2009, respectively.

Since 2009, he has been a Faculty Member and he is currently an Associate Professor with the Department of Electrical Engineering, Indian Institute of Technology Patna, Patna, India. His research interests include nonlinear control theory application to power electronic converters, pulse width modulation techniques, and multiphase electric drives control.

Dr. Behera was the recipient of the 2022 IEEE Outstanding Paper Award for the IEEE TRANSACTIONS ON INDUSTRIAL ELECTRONICS.



Utkal Ranjan Muduli (Senior Member, IEEE) received the B.Tech. degree in electrical and electronics engineering from the Biju Patnaik University of Technology, Rourkela, India, in 2011, the M.Tech. degree in electrical engineering from the Indian Institute of Technology Gandhinagar, India, in 2014, and the Ph.D. degree in electrical engineering from the Indian Institute of Technology Patna, Patna, India, in 2022.

He was a Visiting Scholar and a Research Associate with the Department of Electrical Engineering and Computer Science, Khalifa University, Abu Dhabi, UAE, in 2019 and 2021, respectively, where he is currently a Postdoctoral Research Fellow. His research interests include modulation strategies for multiphase motor drives, matrix converters and its control, battery power management, and wireless power transfer.

Dr. Muduli was the recipient of the 2022 IEEE Outstanding Paper Award for the IEEE TRANSACTIONS ON INDUSTRIAL ELECTRONICS.